Joule

CellPress

Article

Stable pure-iodide wide-band-gap perovskites for efficient Si tandem cells via kinetically controlled phase evolution

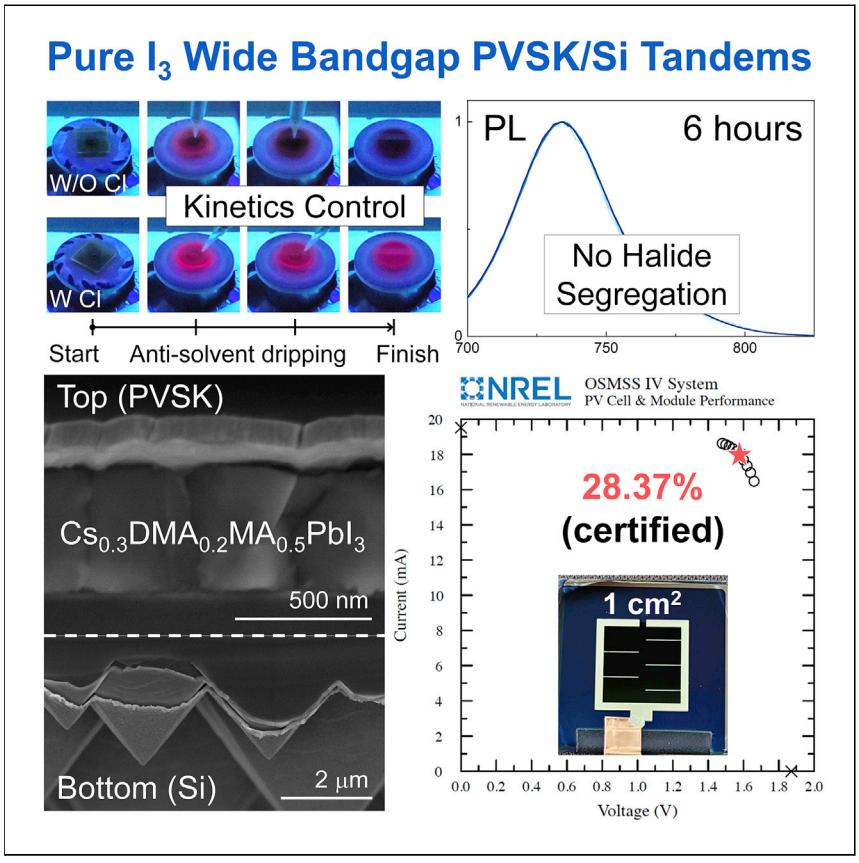

Halide-segregation-free pure-iodide wide-band-gap perovskite films can be prepared via a kinetically controlled phase-evolution route by adding Cl anions. The Cl anions successfully suppress the δ-$CsPbI_3$ phase, which originates from the different nucleation tendency between cations, by forming a two-dimensional Ruddlesden-Popper $Cs_2PbI_2Cl_2$ intermediate phase instead of the δ phase. The resulting pure-iodide perovskite devices exhibit excellent photo-stability (<1% degradation after 1,000 h) and a high tandem efficiency (29.4% in-house, 28.37% certified).

Su Geun Ji, Ik Jae Park, Hogeun Chang, ..., Jungwon Park, Dong Hoe Kim, Jin Young Kim

jungwonpark@snu.ac.kr (J.P.)
donghoekim@korea.ac.kr (D.H.K.)
jykim.mse@snu.ac.kr (J.Y.K.)

Highlights

Fast precipitation of Cs ions is found to induce the δ-$CsPbI_3$ secondary phase

MACl is essential for forming pure-iodide wide-band-gap perovskites without δ phases

Pure-iodide perovskite films show excellent stability without halide-segregation

The best perovskite/Si tandem cell exhibits a high certified efficiency of 28.37%

Ji et al., Joule 6, 1–16
October 19, 2022
https://doi.org/10.1016/j.joule.2022.08.006

Please cite this article in press as: Ji et al., Stable pure-iodide wide-band-gap perovskites for efficient Si tandem cells via kinetically controlled phase evolution, Joule (2022), https://doi.org/10.1016/j.joule.2022.08.006

Joule

CellPress

Article

Stable pure-iodide wide-band-gap perovskites for efficient Si tandem cells via kinetically controlled phase evolution

Su Geun Ji,[1,10] Ik Jae Park,[2,8,10] Hogeun Chang,[3,7,9,10] Jae Hyun Park,[1,4] Geon Pyo Hong,[1] Back Kyu Choi,[3,7] Jun Ho Jang,[1] Yeo Jin Choi,[1] Hyun Woo Lim,[1] You Jin Ahn,[1] So Jeong Park,[1] Ki Tae Nam,[1] Taeghwan Hyeon,[3,7] Jungwon Park,[3,7,*] Dong Hoe Kim,[5,*] and Jin Young Kim[1,4,6,11,*]

SUMMARY

Halide perovskites, promising top-cell materials for efficient Si tandem solar cells, suffer from halide segregation, which results from the halide mixing necessary for achieving band-gap widening. We report pure-iodide wide-band-gap perovskite top cells that are fundamentally free of halide segregation. Cs and dimethylammonium cations were incorporated simultaneously into the A-site of perovskite structure to increase the band gap while maintaining the tolerance factor. However, the incorporation of dual cations resulted in the simultaneous formation of orthorhombic and hexagonal secondary phases rather than forming the pure perovskite phase, owing to the different precipitation kinetics between cations. We demonstrated that this strategy can only be implemented by the phase-controlled nucleation of the Cs-rich composition that governs the desired phase evolution. The pure-iodide perovskite top cell exhibited excellent photo-stability (1% degradation after 1,000 h of continuous operation; ISOS-L-1I, white LED), and its Si tandem exhibited a high conversion efficiency of 29.4% (28.37% certified).

INTRODUCTION

The power conversion efficiency (PCE) of the perovskite solar cells has been improved to 25.7%, which is the highest among all multi-crystalline solar cells and is gradually approaching to the Shockley-Queisser (SQ) limit.[1] Therefore, perovskite-based tandem solar cells are currently attracting significant interest as potential candidates for overcoming the SQ limit of single junction.[2] Among various perovskite-based tandem cells, the perovskite/Si tandem is the most attractive combination because its highest certified PCE (31.3%) has already surpassed that of the best-reported single-junction solar cell (GaAs, 29.1%).[1,3–13] Given the fixed band gap of Si (1.1 eV), the band gap of the best perovskite single-junction device (~1.5 eV) must be increased to approximately 1.7 eV.[14] The band gap of the perovskites can be easily increased by substituting iodine in the X-site of the ABX_3 structure with bromine.[15] However, the resulting mixed-halide perovskites suffer from the critical photo-instability issue of phase segregation into I-rich and Br-rich phases under light illumination.[16] Various strategies, including reduction in Br content,[6,17–19] charge-selective layer engineering,[3] defect passivation,[13,20] and the morphology control[21] have been employed to suppress the phase segregation of mixed-halide perovskites. Nonetheless, complete suppression of the halide segregation in

CONTEXT & SCALE

Expectations to the commercialization of the perovskite/Si tandem solar cell are higher than ever due to its skyrocketing efficiency, but the stability issues still pose a big hurdle. One of the critical stability issues is the segregation of multiple halogen anions that are essential to the wide band gap of the perovskite top cells. The fundamental solution to the halide segregation issue is to use a single-halogen element, but no one so far has demonstrated the single-halide perovskite top cell due to the inevitable formation of secondary phases originating from the precipitation kinetics. Here, we demonstrate wide-band-gap perovskite top cells with a single-halogen element of iodine via a new kinetically controlled phase-evolution path by adding Cl anions. The formation of a new two-dimensional intermediate phase is essential to the kinetics control. The resulting perovskite top cells with pure iodine exhibit significantly enhanced photo-stability and a high tandem efficiency over 29%.

Please cite this article in press as: Ji et al., Stable pure-iodide wide-band-gap perovskites for efficient Si tandem cells via kinetically controlled phase evolution, Joule (2022), https://doi.org/10.1016/j.joule.2022.08.006

mixed-halide perovskites is fundamentally difficult because of the low activation energy associated with halide-ion migration.[22,23] Therefore, the most straightforward and effective way to eliminate this photo-instability issue is to use wide-band-gap perovskites with a single halogen element.[24]

The band gap of pure-iodide perovskites can be increased by substituting Cs cations into the A-site, as evidenced by the wide band gap (1.73 eV) of $CsPbI_3$.[25] However, this method has a critical drawback: the tolerance factor (TF) decreases with the increasing Cs content[26] because of the small ionic radius of the Cs cation compared with that of conventional organic cations, such as methylammonium (MA) or formamidinium (FA). The perovskite structure becomes unstable when the TF decreases excessively (e.g., <0.9), inducing unwanted orthorhombic (δ_O) secondary phases and poor photovoltaic performances.[25,26] The structural instability issue is particularly significant in top-cell applications of Si tandems because considerable amounts of Cs cations should be incorporated into the perovskite structure to achieve a wide band gap. Therefore, introducing Cs cations along with larger cations such as dimethylammonium (DMA) and FA is a rational strategy for maintaining an appropriate TF (0.9–1.0). However, only a few attempts have been made to compensate for the low TF of Cs-based pure-iodide perovskites using large cations, and the photovoltaic performance of these perovskites is inferior to that of typical mixed-halide wide-band-gap perovskites.[27–30] To successfully incorporate multiple cations with considerably different ionic radii (e.g., Cs and DMA) into a single phase and thus prevent the formation of secondary phases, it is crucial to investigate and control the nucleation kinetics and thermodynamics of pure-iodide perovskites. Investigation of the crystallization kinetics is particularly important for the perovskite typically fabricated through solution-based process because each cation in the coating solution exhibits different levels of activity, solubility, and super-saturation. For instance, Cs cations are known to exhibit significantly less solubility than organic cations and are not likely to form intermediate phases during the crystallization process, unlike organic cations.[31,32]

In this work, we developed stable pure-iodide wide-band-gap perovskites with triple cations (i.e., Cs, DMA, and MA) for photo-stable perovskite/Si tandems. We found that the formation of δ_O-$CsPbI_3$ secondary phase is inevitable due to the difference between the precipitation kinetics of each cation, although large cations are co-added to compensate for the low TF of the high Cs compositions. Using Cl anions, however, the two-dimensional (2D) Ruddlesden-Popper (RP) phase ($Cs_2PbI_2Cl_2$) formed instead of the δ_O-$CsPbI_3$ secondary phase in the early stage of the crystallization, which subsequently lead to the formation of the pure-iodide wide-band-gap perovskite films with the desired composition and band gap while successfully suppressing the secondary phases. Our mechanistic investigation elucidated the origin of the inevitable formation of the δ_O-$CsPbI_3$ secondary phase and its successful suppression by the addition of the Cl anions, which further supports the controlled phase evolution by the Cl anions. The single-junction wide-band-gap perovskite solar cell with a high PCE of 20.18% (20.16% certified) exhibited excellent stability by retaining 99% of its initial PCE after 1,000 h of continuous operation (ISOS-L-1I, white LED light source) and was successfully integrated with a Si bottom cell, resulting in the development of an efficient perovskite/Si tandem solar cell with a high PCE of 29.4% (28.37% certified).

RESULTS AND DISCUSSION

Suppression of secondary phases in pure-iodide wide-band-gap perovskites

Figures 1A and S1 show the effect of cation composition on the band gap of $Cs_xDMA_yMA_{1-x-y}PbI_3$ films. The band gap increased from 1.59 to 1.69 eV as the

[1]Department of Materials Science and Engineering, Seoul National University, Seoul 08826, Republic of Korea

[2]Department of Applied Physics, Sookmyung Women's University, Seoul 04310, Republic of Korea

[3]Center for Nanoparticle Research, Institute for Basic Science (IBS), Seoul 08826, Republic of Korea

[4]Research Institute of Advanced Materials (RIAM), Seoul National University, Seoul 08826, Republic of Korea

[5]Department of Materials Science and Engineering, Korea University, Seoul 02841, Republic of Korea

[6]Institute of Engineering Research, College of Engineering, Seoul National University, Seoul 08826, Republic of Korea

[7]School of Chemical and Biological Engineering, Institute of Chemical Process, Seoul National University, Seoul 08826, Republic of Korea

[8]Institute of Advanced Materials and Systems, Sookmyung Women's University, Seoul 04310, Republic of Korea

[9]Present address: QD Lab, Samsung Advanced Institute of Technology, Samsung Electronics, Suwon 16678, Republic of Korea

[10]These authors contributed equally

[11]Lead contact

*Correspondence: jungwonpark@snu.ac.kr (J.P.), donghoekim@korea.ac.kr (D.H.K.), jykim.mse@snu.ac.kr (J.Y.K.)

https://doi.org/10.1016/j.joule.2022.08.006

Please cite this article in press as: Ji et al., Stable pure-iodide wide-band-gap perovskites for efficient Si tandem cells via kinetically controlled phase evolution, Joule (2022), https://doi.org/10.1016/j.joule.2022.08.006

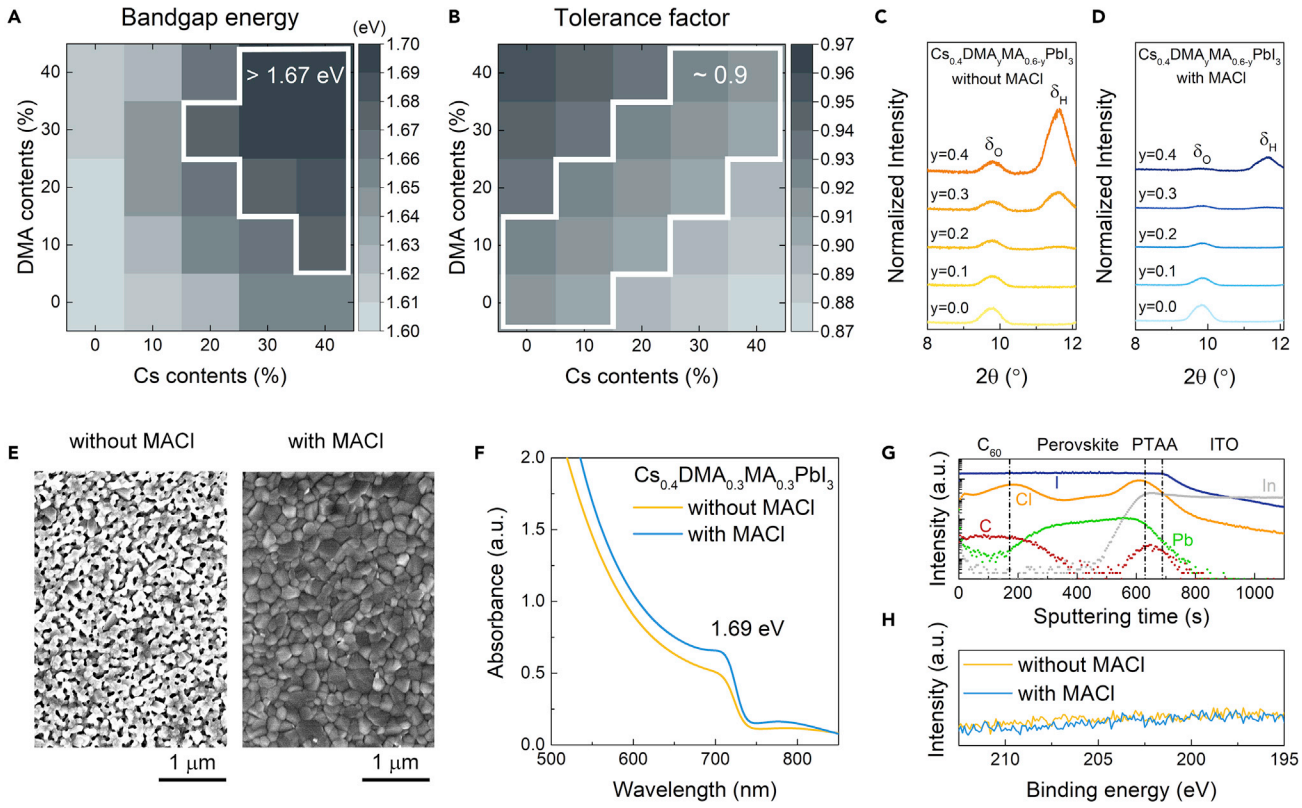

Figure 1. Phase control of pure-iodide wide-band-gap perovskite using MACl additive

(A and B) Optical band gap (A) and calculated tolerance factor (B) of $Cs_xDMA_yMA_{1-x-y}PbI_3$ perovskite films.

(C and D) XRD patterns of $Cs_{0.4}DMA_yMA_{0.6-y}PbI_3$ perovskite films (y = 0–0.4) without (C) and with 15 mol % MACl additive (D).

(E) Top-view SEM images of $Cs_{0.4}DMA_{0.3}MA_{0.3}PbI_3$ perovskite films; left: without MACl, right: with MACl.

(F) Absorption spectrum of $Cs_{0.4}DMA_{0.3}MA_{0.3}PbI_3$ perovskite films without and with MACl.

(G) TOF-SIMS depth profiles of perovskite photovoltaics with MACl-added pure-iodide wide-band-gap perovskite absorber.

(H) XPS analysis of perovskite films showing that no Cl anions were detected (Cl 2p spectrum).

Cs and DMA contents increased from 0% (i.e., $MAPbI_3$) to 40% (i.e., $Cs_{0.4}DMA_{0.4}MA_{0.2}PbI_3$). The compositions that provide the optimal top-cell band gap of 1.67–1.69 eV are indicated with a white line in the contour map (Figure 1A). Figure 1B presents the calculated TFs of the same $Cs_xDMA_yMA_{1-x-y}PbI_3$ perovskites with various Cs and DMA contents. From the TF contour map, it can be expected that increasing the Cs content without adding DMA cations (i.e., y = 0) would result in the formation of δ_O secondary phases because TF would drop below 0.9, which was experimentally confirmed by observing its characteristic peak at 9.8° through X-ray diffraction (XRD) analysis (Figure S2). In contrast, the TF of the $MAPbI_3$ does not change significantly if similar amounts of DMA cations are added along with the Cs cations (white line in Figure 1B) because of the appropriate difference between the ionic radii of Cs (167 pm) and DMA (272 pm) cations (cf. MA 217 pm). Therefore, the formation of δ_O secondary phases due to high Cs compositions (i.e., $x \geq 0.3$) would be suppressed if a sufficient amount of DMA cations is introduced (e.g., $y \geq 0.2$).

However, TF compensation could not be achieved simply by adding DMA cations along with Cs cations. Figure 1C shows that the δ_O secondary phase in the $Cs_{0.4}DMA_yMA_{0.6-y}PbI_3$ film was prominent even when the DMA content increased up to 40%. Furthermore, a hexagonal (δ_H) secondary phase (at 11.7°) appeared for

Please cite this article in press as: Ji et al., Stable pure-iodide wide-band-gap perovskites for efficient Si tandem cells via kinetically controlled phase evolution, Joule (2022), https://doi.org/10.1016/j.joule.2022.08.006

DMA contents over 20%. Interestingly, the synergistic effect of DMA and Cs on the TF only occurred in the presence of methylammonium chloride (MACl) additive. Figure 1D shows the effect of the MACl additive on the phase evolution of the composition shown in Figure 1C. In the presence of the 15 mol % MACl, the peak intensity of the δ_O secondary phase clearly decreased with increasing DMA contents, resulting in an essentially pure perovskite phase under a DMA content of 30%. The δ_O secondary phase still exists in the films with less MACl, indicating that a certain amount of MACl is required to fully suppress the secondary phase (Figure S3). The effect of MACl is believed to be general, as the same phenomena are observed for the films with higher Cs contents and different solvent (Figure S4). The suppression of the secondary phases by MACl can also be observed in the scanning electron microscopy (SEM) images of the $Cs_{0.4}DMA_yMA_{0.6-y}PbI_3$ films (Figures 1E and S5), where the improved film morphology can be considered an added benefit of using the MACl additive.[33] The optical band gap (i.e., 1.69 eV), measured via ultraviolet-visible (UV-vis) spectroscopy, was barely influenced by MACl (Figures 1F and S6), but the steeper absorption edge with the MACl additive indicates the enhanced crystallinity and reduced sub-band-gap trap states.[34]

To identify the contributions of the MA cation and the Cl anion to suppressing secondary phases, we further investigated the effect of MA-based additives with different anions (i.e., Br, I, and SCN) on the phase evolution of the $Cs_{0.4}DMA_{0.3}MA_{0.3}PbI_3$ films. The XRD patterns (Figure S7) show that none of the additives could effectively suppress the secondary phases, confirming that the effect of the MACl additive is solely due to the Cl anions. Residual Cl anions are detected on the top and bottom surface of perovskite layer by the time-of-flight secondary ion mass spectrometry (TOF-SIMS) depth profile, but no evidence of Cl residues can be observed in the X-ray photoelectron spectroscopy (XPS) analysis, even at the top surface (Figures 1G and 1H). The ion chromatography analysis also revealed that the Cl-to-I ratio in the perovskite thin film decreased to 0.3% after annealing, whereas that in the as-spun film was 4.75% that is comparable with the precursor composition (Figure S8). These results confirm that most of the Cl anions escape during the annealing process, and only trace amounts remain at the interfaces, which can be ascribed to the volatile characteristic of MACl[35,36] and low solubility of the Cl anions in iodide-based perovskites.[36–38]

Kinetically controlled phase evolution by Cl anions

To assess the role of Cl anions as a key element for suppressing secondary-phase formation in perovskite with high Cs composition, the precipitation and crystallization behaviors of Cs-containing perovskite solutions with and without Cl anions were investigated. The super-saturation for precipitation was induced either using the inverse temperature crystallization (ITC) method or by injecting an anti-solvent, and the resulting crystals were collected for the further analysis. The ITC method is particularly helpful for investigating the initial precipitation kinetics because the degree of super-saturation gradually increases as opposed to the anti-solvent dripping during the film fabrication. Yellow crystals were precipitated at the early stage of the precipitation (i.e., at 60°C) in the Cs-containing ($Cs_{0.1}MA_{0.9}PbI_3$) solution, whereas no apparent changes were observed in the pure-MA solution (Figure S9). The yellow crystals did not disappear even at the elevated temperature of 80°C. Interestingly, the yellow crystals exhibited diffraction peaks associated with the δ_O-$CsPbI_3$ secondary phase, despite the relatively small amount of Cs cations in the precursor solution (Figure 2A). This indicates that the Cs cations precipitated more preferentially than the MA cations did, which can be further supported by hydrogen nuclear magnetic resonance (H-NMR) and *in-situ* transmission electron microscopy (TEM) analyses (Figures S10–S12; Note S1; Videos S1 and S2). Such a Cs-rich composition and

Please cite this article in press as: Ji et al., Stable pure-iodide wide-band-gap perovskites for efficient Si tandem cells via kinetically controlled phase evolution, Joule (2022), https://doi.org/10.1016/j.joule.2022.08.006

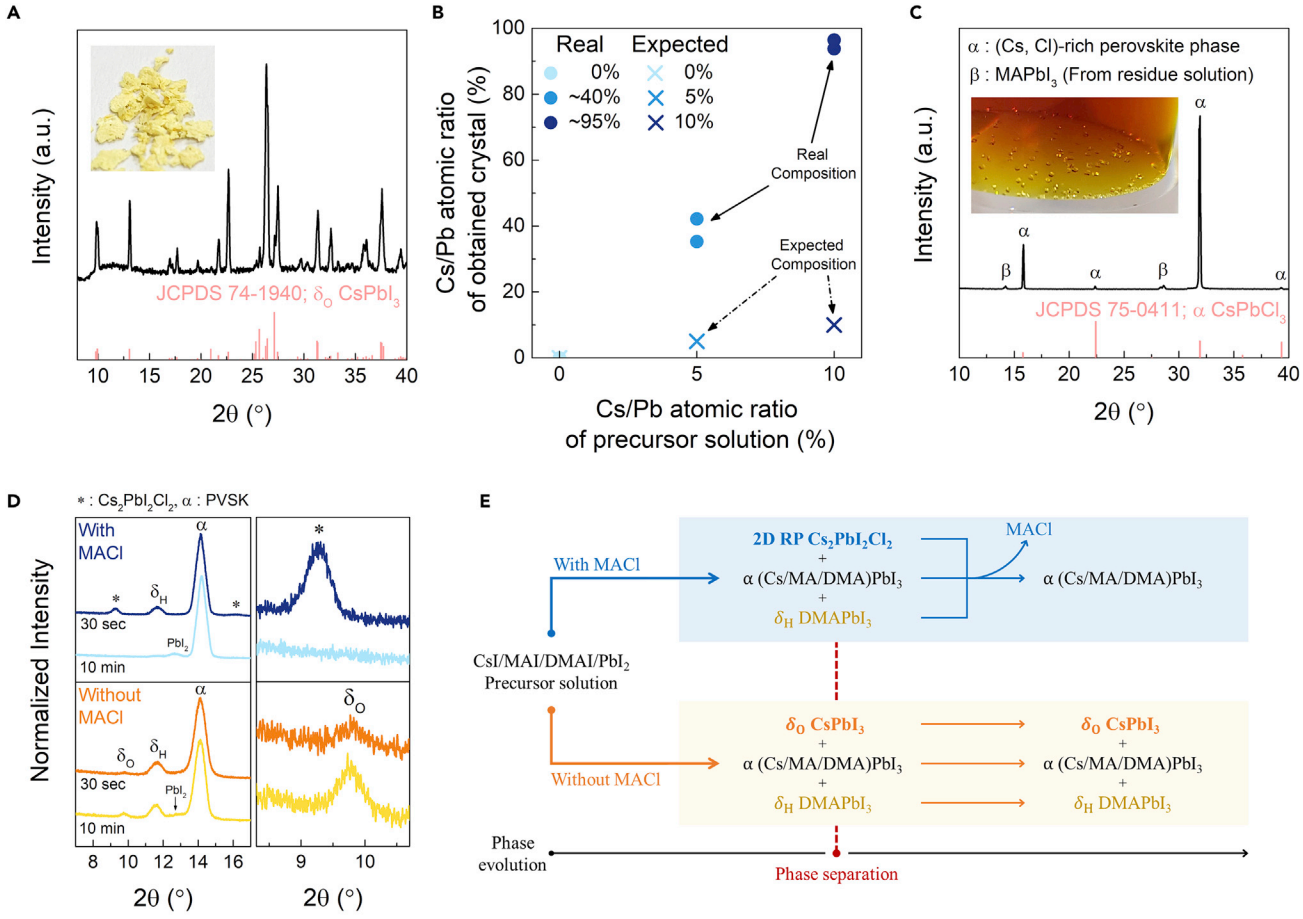

Figure 2. Analysis of different precipitation kinetics of ions and kinetically controlled phase evolution pathway by Cl anions

(A) Powder XRD pattern of preferentially precipitated yellow crystals in $Cs_{0.1}MA_{0.9}PbI_3$ perovskite solution; inset shows the obtained powder.

(B) Inductively coupled plasma mass spectrometry (ICP-MS) analysis of perovskite-phase single crystals grown in different perovskite solution ($MAPbI_3$, $Cs_{0.05}MA_{0.95}PbI_3$, $Cs_{0.1}MA_{0.9}PbI_3$) via seed-assisted ITC. The filled circles are real composition of obtained single crystal, and the crosses are expected composition (i.e., composition of used solution).

(C) Powder XRD pattern of the obtained crystals from $Cs_{0.1}MA_{0.9}Pb(I_{0.9}Cl_{0.1})_3$ perovskite solution, which matches that of the $CsPbCl_3$ perovskite phase; inset shows the obtained transparent crystals.

(D) XRD patterns of short and full annealed $Cs_{0.4}DMA_{0.3}MA_{0.3}PbI_3$ perovskite films with and without MACl additives. Right graph shows the magnified view of peaks between 9° and 10°.

Please cite this article in press as: Ji et al., Stable pure-iodide wide-band-gap perovskites for efficient Si tandem cells via kinetically controlled phase evolution, Joule (2022), https://doi.org/10.1016/j.joule.2022.08.006

Figure 2. *Continued*

(E) Schematic diagram of phase evolution during perovskite film fabrications with and without MACl additive.

(F) Series images of $Cs_{0.4}DMA_{0.3}MA_{0.3}PbI_3$ perovskite-film evolution through the anti-solvent dripping process. Observations were conducted under UV illumination to identify the photo-active perovskite phase based on PL characteristics.

the resulting low TF are responsible for the formation of the δ_O secondary-phase crystals. It is noticeable that the DMA cations did not affect the initial precipitation behavior presumably due to the slow precipitation tendency (Figure S13). The same precipitation experiments were performed in the presence of $MAPbI_3$ seed crystals to exclude the influence of different thermodynamic parameters like the energy barrier for homogeneous nucleation between perovskite and δ_O secondary phases. Like the ITC experiments without the seed crystals, the Cs cations were preferentially precipitated, leading to a much higher Cs-to-MA ratio in the precipitates than that in the solution (i.e., 40% and 95% precipitates from 5% and 10% solutions, respectively; Figures 2B and S14; Note S2). In the presence of the Cl anions, on the other hand, transparent crystals consisting primarily of $CsPbCl_3$ with the perovskite structure (i.e., α phase) were precipitated from $Cs_{0.1}MA_{0.9}Pb(I_{0.9}Cl_{0.1})_3$ solution instead of the yellow δ_O secondary-phase crystals (Figure 2C), which was also observed with different solvents (Figure S15) and in the presence of the DMA cations (Figure S16). This result is interesting considering the relatively small amounts of Cl anions in the precursor solution and suggests that the Cl anions have a strong precipitation tendency as well. The preferential precipitation of Cl anions over that of I anions was demonstrated even without Cs cations as observed from the ITC experiment conducted using the $MAPb(I_{0.5}Cl_{0.5})_3$ solution (Figures S17 and S18). Therefore, the co-addition of Cl anions is believed to form Cs-/Cl-rich nuclei at the early stage of the crystallization process rather than forming the Cs-rich δ_O secondary phase due to their precipitation tendency as fast as Cs cations.

We further investigated the phase evolution in the perovskite films at the early stage of the annealing process. The XRD patterns displayed in Figure 2D show interesting differences depending on the presence of MACl. Without MACl, the δ_O and δ_H phases coexist along with the perovskite phase at the early stage of the annealing process, and all of the three phases are remaining even after the full annealing. In the presence of MACl, on the other hand, no δ_O phase can be observed at the early stage of the annealing process. Instead, the 2D RP mixed-halide phase ($Cs_2PbI_2Cl_2$, Figure S19)[39] newly appears (9.2°, 16.2°) along with the δ_H and perovskite phases. The 2D RP and hexagonal phases disappear after the full annealing, indicating the possibility of the solid-state reaction among three phases to form the pure-iodide perovskite phase. A schematic diagram shown in Figure 2E proposes phase-evolution pathways depending on the presence of Cl anions based on our experimental results. The different precipitation kinetics between ions was found to induce phase separation into Cs-rich phase (i.e., δ_O and $Cs_2PbI_2Cl_2$ without and with MACl, respectively) and DMA-rich phase (i.e., δ_H) in early crystallization process, where the formation of the 2D RP phase instead of the δ_O phase is crucial for achieving the pure perovskite phase.

Figure 2F displays the apparent changes in luminescence of the perovskite films under UV illumination during the initial 4 s after dripping of the anti-solvent. The coating environments are identical to those in the film fabrication process, where the films are spun for approximately 4 s after the anti-solvent dripping before being transferred for annealing. In the absence of Cl anions, a red luminescence appears momentarily (<0.1 s) after dripping of the anti-solvent and then disappeared promptly. However, strong luminescence persists throughout the spinning period

Please cite this article in press as: Ji et al., Stable pure-iodide wide-band-gap perovskites for efficient Si tandem cells via kinetically controlled phase evolution, Joule (2022), https://doi.org/10.1016/j.joule.2022.08.006

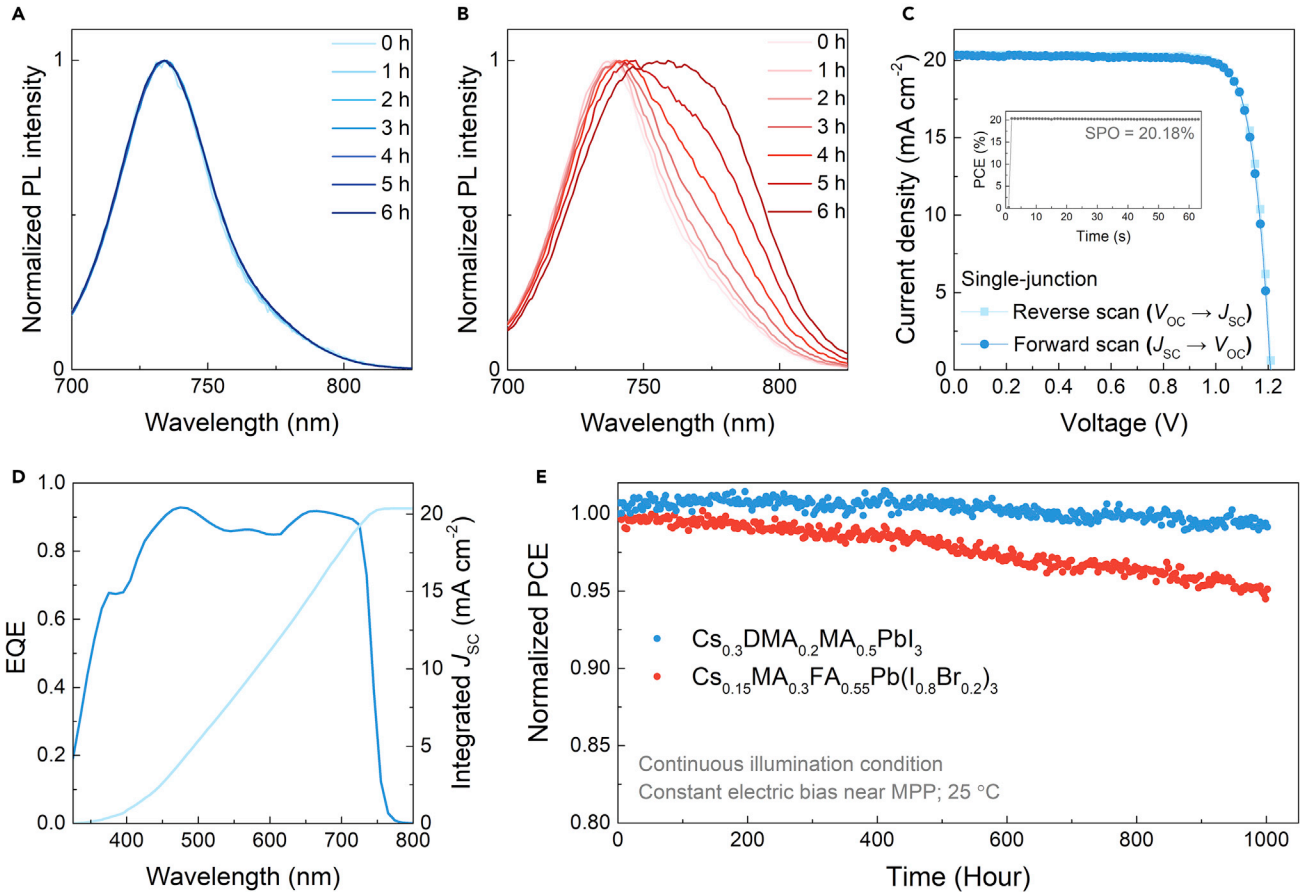

Figure 3. Photovoltaic performances and stability of pure-iodide wide-band-gap perovskite solar cells

(A and B) PL spectrum changes under continuous laser irradiation of MACl-added $Cs_{0.3}DMA_{0.2}MA_{0.5}PbI_3$ (A) and $Cs_{0.15}MA_{0.3}FA_{0.55}Pb(I_{0.8}Br_{0.2})_3$. (B) perovskite films with a similar band gap.

(C) *J-V* curves of best-performing single-junction perovskite solar cell fabricated with MACl-added $Cs_{0.3}DMA_{0.2}MA_{0.5}PbI_3$ perovskite. Inset shows the SPO measurement result under the MPP condition.

(D) EQE spectrum of best-performing device (blue line) and its integrated J_{SC} (cyan line).

(E) Long-term stability of semi-transparent perovskite solar cells fabricated with $Cs_{0.3}DMA_{0.2}MA_{0.5}PbI_3$ and $Cs_{0.15}MA_{0.3}FA_{0.55}Pb(I_{0.8}Br_{0.2})_3$ perovskites under continuous-operation condition (ISOS-L-1I, white LED light source).

in the presence of the Cl anions. It should be noted that no difference between the films was observed during spin-coating under an ambient light (Figure S20; Videos S3, S4, S5, and S6). The different luminescent behaviors indicate that intermediate phases with completely different photoelectric properties formed depending on the presence of Cl anions. The steady-state photoluminescence (PL) measurement of the as-spun films revealed that the PL intensity without Cl anions is much lower than that with Cl anions (Figure S21), which can be ascribed to the formation of δ_O-$CsPbI_3$ phase with an indirect band gap[27] of 2.82 eV. Conversely, the strong red PL with Cl anions indicates that the formation of the δ_O secondary phase is successfully prevented by forming the 2D RP $Cs_2PbI_2Cl_2$ phase, which is consistent with the solution precipitation experiments and XRD results.

Photo-stability of pure-iodide perovskite materials and devices

To confirm the photo-stability of the pure-iodide perovskites, steady-state PL spectra of the perovskite films without encapsulation were plotted as a function of time under continuous laser irradiation in ambient condition (Figures 3A and 3B;

Please cite this article in press as: Ji et al., Stable pure-iodide wide-band-gap perovskites for efficient Si tandem cells via kinetically controlled phase evolution, Joule (2022), https://doi.org/10.1016/j.joule.2022.08.006

Table 1. Photovoltaic parameters of the best-performing pure-iodide wide-band-gap perovskite single-junction solar cell and perovskite/Si double-junction tandem solar cell

	J_{SC} (mA cm^{-2})	V_{OC} (V)	PCE (%)	FF (%)
Opaque cell (reverse scan), 0.14 cm^2	20.30	1.21	20.18	82.1
Opaque cell (forward scan), 0.14 cm^2	20.30	1.21	20.15	82.0
Tandem cell (reverse scan), 1.0 cm^2	19.82	1.89	29.60	79.0
Tandem cell (forward scan), 1.0 cm^2	19.80	1.90	29.51	78.4

room temperature, relative humidity ≈30%). $Cs_{0.3}DMA_{0.2}MA_{0.5}PbI_3$ films were used for the further characterization of materials and devices because their band gap (1.68 eV; Figure S22) matches best with that of the Si bottom cell for tandem. We observed that 10 mol % MACl was sufficient for suppressing the formation of secondary phases. $Cs_{0.15}MA_{0.3}FA_{0.55}Pb(I_{0.8}Br_{0.2})_3$ films with the same band gap were used as control samples. The PL spectrum of the pure-iodide wide-band-gap perovskite film did not change even after continuous laser irradiation for 6 h (Figure 3A), thereby signifying the excellent photo-stability. In contrast, the PL spectrum of the mixed-halide wide-band-gap perovskite film underwent an apparent red shift, which is clear evidence of light-induced phase segregation of the mixed-halide perovskite (Figure 3B).[16]

The photovoltaic properties of the pure-iodide wide-band-gap perovskite were investigated using a single-junction p-i-n solar cell consisting of stacked multiple layers of glass/indium tin oxide (ITO)/poly(triarylamine) (PTAA)/perovskite/C_{60}/polyethylenimine (PEIE)/Ag. The addition of MACl was observed to be crucial for ensuring properly functioning solar cells (Figure S23A), likely because of the successful suppression of the secondary phases. Moreover, the photovoltaic performance of the cell was further enhanced using additional additives, as shown in Figure S23B and Table S1. Two additives (lead thiocyanate [$Pb(SCN)_2$] and phenethylammonium thiocyanate [PEASCN]) were used to facilitate the grain growth and the passivation of the grain boundary, respectively.[7,40] As a result, a high PCE of 20.18% with a short-circuit current density (J_{SC}) of 20.30 mA cm^{-2}, an open-circuit voltage (V_{OC}) of 1.21 V, and a fill factor (FF) of 0.821 was achieved, as shown in Figure 3C and Table 1. It exhibited a stabilized power output (SPO) of 20.18% and negligible *J-V* hysteresis. In addition, the integrated J_{SC}, which was obtained from the external quantum efficiency (EQE) spectrum (20.36 mA cm^{-2}), was very close to J_{SC} obtained from the *J-V* curve (Figure 3D). Official test results also showed a similar conversion efficiency of 20.16% (Figure S24).

Figure 3E compares the long-term stability of the pure-iodide wide-band-gap perovskite solar cell with that of its mixed-halide counterpart using a standard measurement condition (ISOS-L-1I).[41] For the long-term stability test, semi-transparent single-junction solar cells were illuminated through their un-encapsulated ITO top electrode using a white LED lamp. The current output under a constant electric bias near the maximum power point (MPP) were recorded at 25°C. The pure-iodide wide-band-gap perovskite solar cell exhibited excellent long-term stability, retaining 99% of its initial PCE even after 1,000 h of continuous operation. In contrast, the PCE of the control device with mixed halides (i.e., 20% of Br) dropped below 95% after 1,000 h, indicating inferior long-term stability. Similar results were observed under a harsher measurement condition of ISOS-L-2I, too (Figure S25). The control device with mixed halides itself shows decent stability compared with previous reports on non-transparent single-junction devices with similar compositions,[42] which can be ascribed to the diffusion barrier effect by the ITO top layer

Please cite this article in press as: Ji et al., Stable pure-iodide wide-band-gap perovskites for efficient Si tandem cells via kinetically controlled phase evolution, Joule (2022), https://doi.org/10.1016/j.joule.2022.08.006

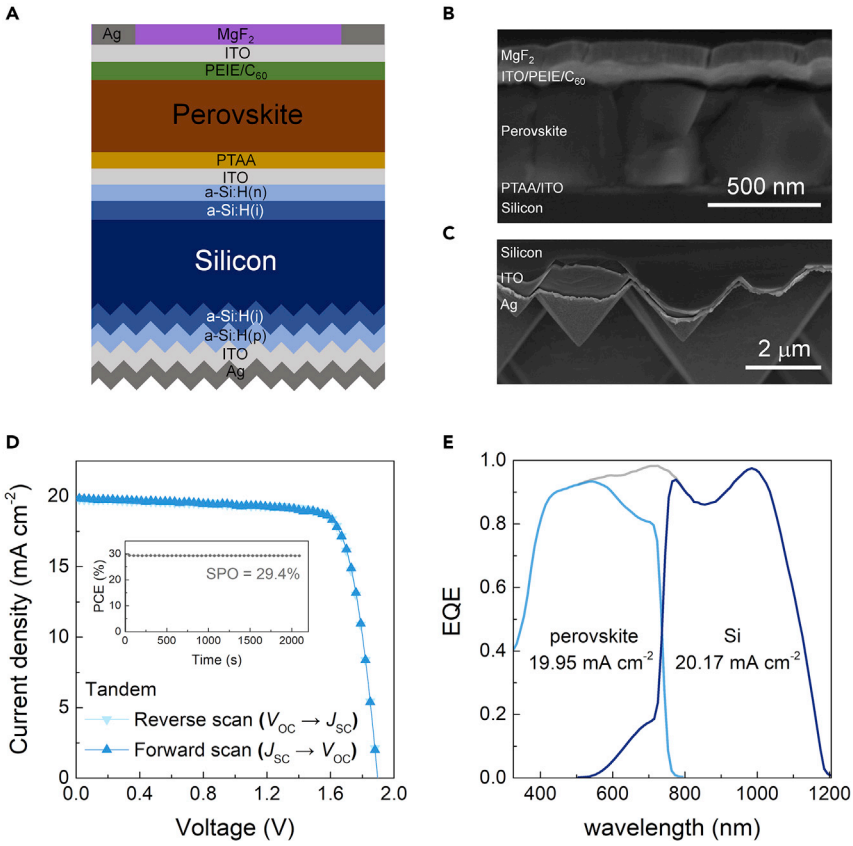

Figure 4. Structure and photovoltaic performances of perovskite/Si 2-terminal monolithic tandem solar cells

(A) Schematic diagram of the structure of perovskite/Si tandem devices.

(B and C) Cross-sectional SEM image of the perovskite top sub-cell (B) and rear textured side of Si bottom sub-cell (C) in the tandem device.

(D) *J-V* curves of the best-performing perovskite/Si tandem solar cell fabricated with the MACl-added $Cs_{0.3}DMA_{0.2}MA_{0.5}PbI_3$ perovskite. Inset shows the SPO measurement result under MPP conditions.

(E) EQE spectrum of each sub-cell of the perovskite/Si tandem device. The blue, dark blue, and gray lines denote the results of the perovskite top sub-cell, Si bottom sub-cell, and the sum of each sub-cell, respectively.

effectively blocking the diffusion of atoms or molecules.[43] It is noteworthy that the pure-iodide wide-band-gap perovskite solar cell showed a decent thermal stability by maintaining over 80% of its initial PCE after 1,000 h under thermal stress condition, although it incorporates MA cations (Figure S26). No evidence of the thermal decomposition like the lead iodide (PbI_2) phase was observed, either.

Highly efficient monolithic perovskite/Si tandem cells

The pure-iodide wide-band-gap perovskite was employed as the top cell of a monolithic perovskite/Si tandem solar cell. The top surface of the textured silicon heterojunction (SHJ) bottom cell was polished for ensuring a uniformity of the perovskite layer fabricated by spin-coating process. Figure 4A presents a schematic structure of the tandem cell, where a 20 nm-thick ITO layer deposited as a recombination layer provides the electrical connection between the two sub-cells. The optimized thickness of the top ITO (40 nm) and C_{60} (15 nm) layers were determined in the preliminary experiments to minimize the optical losses caused by parasitic absorption.[44]

Please cite this article in press as: Ji et al., Stable pure-iodide wide-band-gap perovskites for efficient Si tandem cells via kinetically controlled phase evolution, Joule (2022), https://doi.org/10.1016/j.joule.2022.08.006

Figures 4B and 4C present cross-sectional SEM images of the perovskite top cell and the textured rear contact of the Si bottom cell, respectively. The uniform perovskite layer with a thickness of approximately 500 nm consisted predominantly of single grains oriented in the vertical direction. The best tandem cell exhibited a high PCE of 29.60% with J_{SC} of 19.82 mA cm^{-2}, V_{OC} of 1.89 V, and FF of 0.79, as well as negligible hysteresis and a SPO value of 29.4% (Figure 4D; Table 1). The highest certified efficiency of the tandem cell measured in the National Renewable Energy Laboratory was 28.37% (Figure S27). The *J-V* measurements were performed on an area of 1.00 cm^2 defined by the aperture size. The V_{OC} of the Si bottom cell, which was measured with filtered light using a semi-transparent perovskite solar cell, was 0.70 V. The V_{OC} of the semi-transparent perovskite top cell was 1.20 V (Figure S28). The sum of the V_{OC} values of each sub-cell was exactly equal to the tandem V_{OC}. Figure 4E presents EQE spectrum of the two sub-cells of tandem device. The integrated J_{SC} values of the top and bottom cells were 19.95 and 20.17 mA cm^{-2}, respectively. The limiting current density of the top cell (i.e., 19.95 mA cm^{-2}) is essentially identical (difference of less than 1%) to the matching current density obtained from the *J-V* curve (19.82 mA cm^{-2}). The tandem solar cell exhibits a decent operational stability by maintaining over 98% of the initial PCE after continuous operation for 200 h under ISOS-L-1I condition with white LED light source (Figure S29).

Conclusions

We identified the origin of the δ_O secondary-phase formation in the perovskite films with high Cs compositions and proposed a new phase-evolution pathway for preparing pure-iodide wide-band-gap perovskite films without the secondary phases, for which the controlled precipitation kinetics at the early stage of the crystallization process is essential. The fast precipitation tendency of Cs cations was found to lead to the formation of the δ_O secondary phase, which could be successfully prevented by adding Cl anions having similarly fast precipitation tendency as Cs cations. As a result, pure-iodide wide-band-gap perovskite films with excellent photo-stability, which are fundamentally free from the halide-segregation issue, could be prepared. We also demonstrated highly efficient and stable single-junction and Si tandem solar cells using the pure-iodide perovskite films. Understanding the correlation between the precipitation kinetics of ions and the phase evolution of the films along with the strategy of the kinetically controlled phase evolution will provide new insights for materials design of perovskites with unusual compositions.

EXPERIMENTAL PROCEDURES

Resource availability

Lead contact

Further information and requests for resources and materials should be directed to and will be fulfilled by the lead contact, Jin Young Kim (jykim.mse@snu.ac.kr).

Materials availability

This study did not generate new unique materials.

Data and code availability

This study did not generate any datasets.

Materials

Methylammonium iodide (MAI), methylammonium bromide (MABr), methylammonium thiocyanate (MASCN), dimethylammonium iodide (DMAI), formamidinium iodide (FAI), and PEASCN were purchased from Greatcell Solar. MACl was purchased from Lumtec. PbI_2 was purchased from Alfa Aesar. C_{60} was purchased from nano-c.

Please cite this article in press as: Ji et al., Stable pure-iodide wide-band-gap perovskites for efficient Si tandem cells via kinetically controlled phase evolution, Joule (2022), https://doi.org/10.1016/j.joule.2022.08.006

Cesium iodide (CsI), $Pb(SCN)_2$, PTAA, dimethylformamide (DMF), N-methyl-2-pyrrolidone (NMP), dimethyl sulfoxide (DMSO), DMSO-d_6, toluene, PEIE (80% ethoxylated solution), gamma-butyrolactone (GBL), acetonitrile (ACN), propylene carbonate (PC), lead bromide ($PbBr_2$), magnesium fluoride (MgF_2), and methyl acetate were purchased from Sigma Aldrich.

Fabrication of perovskite films

1.2 M of perovskite precursor solutions were prepared by dissolving CsI, MAI, DMAI, FAI, PbI_2, $PbBr_2$, and MACl ($Cs_xDMA_yMA_{1-x-y}PbI_3$ with z mol % of MACl; $Cs_{0.15}MA_{0.3}FA_{0.55}PbI_{2.4}Br_{0.6}$ for control) in DMF and NMP mixed solvent (DMF:NMP = 4:1; volume ratio). Perovskite precursor solutions contained 1.5 mol % of PEASCN and 2.0 mol % of $Pb(SCN)_2$ for 2D additive included perovskite films. To fabricate perovskite films, precursor solutions were spin-coated on substrate at 3,000 rpm for 24 s. 50 μL of methyl acetate was dripped on wet films at 20 s after start of spinning. After spinning, films were annealed at 100°C for 10 min.

Due to the low solubility of CsI and MACl in NMP, DMF, and DMSO mixed solvents (4:1 volume ratio) were used to prepare high Cs-content perovskite precursors. The concentrations of solution were 0.9 M for $Cs_{0.5}DMA_yMA_{0.5-y}PbI_3$ with 25 mol % of MACl and 0.5 M for $Cs_{0.6}DMA_yMA_{0.4-y}PbI_3$ with 35 mol % of MACl. These high Cs-content perovskite films were spin-coated at 3,000 rpm for 34 s with a methyl acetate dripping at 30 s after start of spinning. As-spun films were annealed at 140°C for 10 min.

Fabrication of single-junction perovskite solar cells

PTAA solution (7 mg/mL in toluene) was spin-coated on ITO substrates at 6,000 rpm for 30 s followed by annealing at 100°C for 10 min. Perovskite solutions were spin-coated on PTAA coated substrates with above-mentioned manner. On the perovskite films, 20 nm-thick C_{60} layer was deposited by thermal evaporation with 0.1 Å/s of deposition rate. PEIE solution (0.2 wt % in methanol) was dynamically spin-coated on C_{60} evaporated substrates at 6,000 rpm for 30 s. For single-junction opaque devices, 120 nm-thick Ag layer was deposited on C_{60}/PEIE layer by thermal evaporation. For single-junction semi-transparent devices, 150 nm-thick ITO layer was deposited by radiofrequency (RF) sputtering at room temperature (base pressure: 2×10^{-6} Torr, working pressure: 2×10^{-3} Torr, power: 50 W). After that, 120 nm-thick Ag grid was deposited on the ITO layer by thermal evaporation. As anti-reflection layers, Moth-eye films (Mitsubishi Chemical) were attached on the top of the semi-transparent perovskite cells.

Fabrication of silicon solar cells

Double side polished 300 μm-thick of n-type phosphor-doped Si wafers were used for Si solar cells prepared by floating zone technique (3.0 Ω cm). To remove contaminants, RCA cleaning process was conducted by immersing substrates in $HCl:H_2O_2$ and $H_2SO_4:H_2O_2$ solutions before the deposition of a-Si:H layers. Then, 2.5 cm × 2.5 cm size substrates were rinsed with deionized (DI) water and dipped in buffered oxide etching solution for removal of native oxide. Parallel-plate direct plasma-enhanced chemical vapor deposition (PE-CVD) was used to deposit 10–20 nm thick of a-Si:H layers in both side of wafer with reactor operating at RF 13.56 MHz power. For doping of a-Si:H layers, hydrogen-diluted PH_3 and B_2H_6 gases were used. After that, a 20 nm-thick ITO layer was deposited for recombination layers on front side of cells. On rear side, an 80 nm-thick ITO layer and a

Please cite this article in press as: Ji et al., Stable pure-iodide wide-band-gap perovskites for efficient Si tandem cells via kinetically controlled phase evolution, Joule (2022), https://doi.org/10.1016/j.joule.2022.08.006

300 nm-thick Ag layer were sequentially deposited with 1.2 cm × 1.2 cm size by sputtering and thermal evaporation respectively.

Fabrication of monolithic perovskite/Si tandem solar cells

On the top of Si bottom cell with ITO recombination layer, PTAA/perovskite/C_{60}/PEIE layers were sequentially deposited with the same manner of single-junction perovskite solar cells. To improve the light harvesting, the thickness of C_{60} layer was reduced to 15 nm. A 40 nm-thick ITO layer was deposited with 1.2 cm × 1.2 cm size by sputtering and a 500 nm-thick, 50 μm-width Ag grid was deposited by thermal evaporation. Finally, a 105 nm-thick MgF_2 layer was deposited on the device by thermal evaporation as an anti-reflection layer. Detailed photo images of the tandem cells are presented in Figure S30.

Precipitation of powder and single crystals from perovskite solutions

To investigate the phase evolution in perovskite solution containing various cations, 0.8 M of $MAPbI_3$, $DMA_{0.1}MA_{0.9}PbI_3$, $Cs_{0.1}MA_{0.9}PbI_3$, $Cs_{0.1}DMA_{0.1}MA_{0.8}PbI_3$, and $Cs_{0.1}DMA_{0.2}MA_{0.7}PbI_3$ perovskite precursor solutions dissolved in GBL were prepared. After that, perovskite precursor solution and ACN were mixed with 1:1 volume ratio.[45] The ACN was used to enhance the temperature dependence of the solubility, so that the temperature for the precipitation can be decreased. The temperature of mixed solutions was gradually raised up from 50°C to 90°C in a silicone oil bath with 5°C/h ramp-up rate. In presence of Cs cation in solutions, yellow crystals were precipitated at 60°C and gathered followed by drying at 35°C in vacuum oven. When the temperature of solution reached 80°C, black perovskite crystals started to precipitated and were gathered by the same method.

For seed-assisted perovskite single crystal growth, 0.8 M of $MAPbI_3$, $Cs_{0.05}MA_{0.95}PbI_3$, and $Cs_{0.1}MA_{0.9}PbI_3$ perovskite precursor solutions dissolved in GBL were prepared. Perovskite precursor solutions were mixed with ACN (2:1 volume ratio), and prepared $MAPbI_3$ seed crystals were transferred into each mixed solution. The temperature of solutions with crystal seeds was gradually raised up 80°C–120°C and grown crystals in solutions were gathered and dried by the same method.

To investigate the phase evolution in presence of Cl anions in the precursor solution, 1.2 M of $Cs_{0.1}MA_{0.9}PbI_3$, $Cs_{0.1}MA_{0.9}Pb(I_{0.9}Cl_{0.1})_3$ and $Cs_{0.1}DMA_{0.1}MA_{0.8}Pb(I_{0.9}Cl_{0.1})_3$ perovskite precursor solutions dissolved in DMF and GBL mixed solvent (1:1 volume ratio) were prepared. After that, perovskite precursor solution and ACN were mixed (2:1 volume ratio). Since the solubility of the solutes is a little different from that in the absence of Cl, the temperature of perovskite solutions was raised up to 120°C for the complete dissolution of solute first. Then, a silicone oil bath was gradually cooled to 60°C with 5°C/h rate. The solutions were kept at 60°C for a day, and grown crystals were gathered followed by drying at 35°C in vacuum oven. A same experiment was conducted by DMF and NMP mixed solvent with 4:1 volume ratio (2.4 M of $Cs_{0.1}MA_{0.9}Pb(I_{0.9}Cl_{0.1})_3$ precursor solution) to study the effect of solvent. This solution was mixed with PC and ACN (1:0.7:0.3 volume ratio).

To study precipitation tendency between I and Cl anions, 2.5 M of $MAPbI_{1.5}Cl_{1.5}$ perovskite precursor solution dissolved in DMF and DMSO mixed solvent (1:1 volume ratio) was prepared.[46] Precursor solutions was gradually heated from 60°C to 90°C in a silicone oil bath with 10°C/day rate. At 70°C, nuclei of perovskite started to be observed and those crystals were gathered after growing for 2 days followed by drying at 35°C in vacuum oven.

Please cite this article in press as: Ji et al., Stable pure-iodide wide-band-gap perovskites for efficient Si tandem cells via kinetically controlled phase evolution, Joule (2022), https://doi.org/10.1016/j.joule.2022.08.006

Characterization

To investigate composition of crystals, H-NMR and inductively coupled plasma mass spectrometry (ICP-MS) were employed. Solutions for H-NMR were prepared by dissolving precipitated powder in DMSO-d_6 (JeolJNM-LA400, JEOL). Solutions for ICP-MS were prepared by dissolving precipitated powder and single crystals in HCl and DI water mixed solution (HCl:DI water = 1:1 volume ratio, JP/7900 ICP-MS, Agilent). Solutions for the ion chromatography analysis were prepared by dissolving powders scraped from thin films in a mixed solution of HBr and DI water (HBr:DI water = 1:60 volume ratio, ICS-3000, Dionex). Structural analysis of films, powder, and single crystals were investigated by XRD and HRXRD with Cu Kα radiation (XRD; New D8 Advance, Bruker, HRXRD; SmartLab, Rigaku). Optical properties of films and single crystals were measured by UV-vis spectroscopy (Cary5000, Agilent). The top-view and cross-sectional images of films and devices were examined by SEM (SU70, Hitachi). For investigation of residue Cl anions in perovskite films, XPS was conducted (SIGMA PROBE, ThermoFisher Scientific). Additionally, TOF-SIMS depth profiles of elements were measured by Cs ion beam sputtering (TOF SIMS-5, ION-TOF). PL changes of perovskite films were investigated by measuring PL spectrum periodically at room temperature under ambient atmosphere condition with continuous 520 nm laser illumination whose laser power is 2.5 mW with 1.5 mm × 3.5 mm of elliptical beam shape (FlouTime 300, PicoQuant). *J-V* measurement of single-junction and tandem solar cells were conducted with potentiostat under AM 1.5G illumination (100 mW/cm^2) by solar simulator (potentiostat; CHI 608C, CH Instruments, solar simulator; PEC-L11, Peccell Technologies, AAA graded). The AM 1.5G illumination were calibrated by standard Si cell with quartz filter (91150V, Newport; certified date: February 2017). The *J-V* measurements were conducted with aperture whose size are 0.14 and 1.00 cm^2 by metal mask for single-junction devices and tandem devices, respectively. The scan rates of *J-V* were 120 and 240 mV/s for single-junction devices and tandem devices, respectively. The *J-V* scans were conducted in ambient atmosphere at room temperature without any preconditioning such as light soaking. The EQE spectrum of single-junction devices were measured without light or electrical bias (QUANTX-300, Oriel). The EQE spectrum of top-cell of tandem devices were measured under infrared light bias condition with 600 mV of electrical bias. The EQE spectrum of bottom-cell of tandem devices were measured under blue light bias condition without electrical bias. Source of light bias was quartz tungsten halogen (QTH) lamp. Colored glass filter (RG.850) was used for infrared light bias, and blue bandpass filter (BG.39) was used for blue light bias. The long-term stability test of semi-transparent wide-band-gap perovskite devices was conducted by continuous illumination white LED (MWWHLP1, THORLABS). Light intensity of LED was adjusted to output same current density at zero bias with that from *J-V*. Under continuous illumination, output current density of devices was recorded with constant electrical bias at near MPP. The devices were operated in home-made N_2-filled chamber at a constant temperature of 25°C using a water cooler and 65°C using a water heater to satisfy the ISOS-L-1I and ISOS-L-2I protocols, respectively. For investigation of tandem device, 940 nm of LED lamp (940P3, THORLABS) were additionally used for compensating the spectrum of the white LED lamp. The thermal stability test of devices was conducted in N_2 glove box, and *J-V* curves were periodically measured under AM 1.5G illumination at room temperature.

In-situ liquid cell TEM analysis

In-situ liquid cell TEM experiment was conducted using JEM-2100F (JEOL). TEM operated at 200 kV, equipped with an UltraScan 1000XP CCP detector (Gatan).

Please cite this article in press as: Ji et al., Stable pure-iodide wide-band-gap perovskites for efficient Si tandem cells via kinetically controlled phase evolution, Joule (2022), https://doi.org/10.1016/j.joule.2022.08.006

The liquid cell consists of a bottom chip (550 × 50 μm window, silicon nitride membrane thickness of 50 nm, and 50 nm spacer) and a top chip (550 × 50 μm window, silicon nitride membrane thickness of 50 nm without spacer). All chips were purchased from Protochips, USA. For sample preparation, ~0.1 μL of 60 mM $Cs_{0.1}MA_{0.9}PbI_3$ or $MAPbI_3$ precursor dissolved in NMP was loaded between the chips. *In-situ* movies were recorded in 10 frames/s with the flow of methyl acetate as an anti-solvent at a rate of 120 μL/h. TEM and corresponding selected area electron diffraction (SAED) images were acquired after the enough reaction with the anti-solvent flow of 1 h.

SUPPLEMENTAL INFORMATION

Supplemental information can be found online at https://doi.org/10.1016/j.joule.2022.08.006.

ACKNOWLEDGMENTS

The authors acknowledge the Energy Business Division, BS Company of LG Electronics for supplying Si bottom cells for the tandem cell fabrication. This work was supported by the National Research Foundation of Korea (NRF) grant funded by Korea government (Ministry of Science and ICT) (no. NRF-2022M3J1A1063226, no. NRF-2021M3H4A1A03057403, and no. NRF-2020R1A2C1102718); LG Display under the LGD-SNU Incubation Program; the Korea Institute of Energy Technology Evaluation and Planning (KETEP) and the Ministry of Trade, Industry & Energy (MOTIE) of the Republic of Korea (no. 20203040010320); The Research Center Program of Institute for Basic Science of Korea (no. IBS-R006-D1); and Samsung Research Funding & Incubation Center of Samsung Electronics (no. SRFC-MA2002-03).

AUTHOR CONTRIBUTIONS

J.Y.K. supervised the project. S.G.J. and J.Y.K. conceived the idea. S.G.J., I.J.P., D.H.K., and J.Y.K. designed the experiments. S.G.J. characterized and synthesized the perovskite materials and fabricated solar cell devices. I.J.P. helped in the fabrication of perovskite/Si double-junction solar cells. H.C., B.K.C., T.H., and J.P. carried out the observation and analysis of crystallization in perovskite solution by *in-situ* TEM. J.H.P. helped in the electrical characterization and certification of solar cell devices. G.P.H. helped in performing optical measurement. Y.J.C. helped in the fabrication of perovskite single-junction solar cells. J.H.P. and H.W.L. helped in the long-term stability tests of devices. J.H.J. conducted the NMR analysis. Y.J.C. and S.J.P. helped in performing XRD measurement. Y.J.A. helped in performing SEM observation. S.G.J., I.J.P., H.C., D.H.K., and J.Y.K. wrote the manuscript. All authors contributed to the discussion of the results, provided feedback, and reviewed the manuscript.

DECLARATION OF INTERESTS

S.G.J., I.J.P., Y.J.A., and J.Y.K. are inventors on a patent (KR 10-2020-0101527) submitted by R&DB Foundation of Seoul National University that covers the pure-iodide wide-band-gap perovskites.

Received: June 9, 2022
Revised: July 21, 2022
Accepted: August 16, 2022
Published: September 19, 2022

REFERENCES

1. National Renewable Energy Laboratory (2022). Best research-cell efficiency chart. www.nrel.gov/pv/cell-efficiency.html.

2. Eperon, G.E., Hörantner, M.T., and Snaith, H.J. (2017). Metal halide perovskite tandem and multiple-junction photovoltaics. Nat. Rev. Chem. *1*, 0095. https://doi.org/10.1038/s41570-017-009510.1038/s41570-017-0095.

3. Al-Ashouri, A., Köhnen, E., Li, B., Magomedov, A., Hempel, H., Caprioglio, P., Márquez, J.A., Morales Vilches, A.B., Kasparavicius, E., Smith, J.A., et al. (2020). Monolithic perovskite/silicon tandem solar cell with >29% efficiency by enhanced hole extraction. Science *370*, 1300–1309. https://doi.org/10.1126/science.abd401610.1126/science.abd4016.

4. Hou, Y., Aydin, E., De Bastiani, M., Xiao, C., Isikgor, F.H., Xue, D.-J., Chen, B., Chen, H., Bahrami, B., Chowdhury, A.H., et al. (2020). Efficient tandem solar cells with solution-processed perovskite on textured crystalline silicon. Science *367*, 1135–1140. https://doi.org/10.1126/science.aaz369110.1126/science.aaz3691.

5. Chen, B., Yu, Z.J., Manzoor, S., Wang, S., Weigand, W., Yu, Z., Yang, G., Ni, Z., Dai, X., Holman, Z.C., et al. (2020). Blade-coated perovskites on textured silicon for 26%-efficient monolithic perovskite/silicon tandem solar cells. Joule *4*, 850–864. https://doi.org/10.1016/j.joule.2020.01.00810.1016/j.joule.2020.01.008.

6. Xu, J., Boyd, C.C., Yu, Z.J., Palmstrom, A.F., Witter, D.J., Larson, B.W., France, R.M., Werner, J., Harvey, S.P., Wolf, E.J., et al. (2020). Triple-halide wide–band gap perovskites with suppressed phase segregation for efficient tandems. Science *367*, 1097–1104. https://doi.org/10.1126/science.aaz507410.1126/science.aaz5074.

7. Kim, D., Jung, H.J., Park, I.J., Larson, B.W., Dunfield, S.P., Xiao, C., Kim, J., Tong, J., Boonmongkolras, P., Ji, S.G., et al. (2020). Efficient, stable silicon tandem cells enabled by anion-engineered wide-bandgap perovskites. Science *368*, 155–160. https://doi.org/10.1126/science.aba343310.1126/science.aba3433.

8. Park, I.J., Park, J.H., Ji, S.G., Park, M.-A., Jang, J.H., and Kim, J.Y. (2019). A three-terminal monolithic perovskite/Si tandem solar cell characterization platform. Joule *3*, 807–818. https://doi.org/10.1016/j.joule.2018.11.01710.1016/j.joule.2018.11.017.

9. Zheng, J., Mehrvarz, H., Ma, F.-J., Lau, C.F.J., Green, M.A., Huang, S., and Ho-Baillie, A.W.Y. (2018). % Efficient monolithic perovskite/homo-junction-silicon tandem solar cell on 16 cm^2. ACS Energy Lett *3*, 2299–2300. https://doi.org/10.1021/acsenergylett.8b0138210.1021/acsenergylett.8b01382.

10. Bush, K.A., Palmstrom, A.F., Yu, Z.J., Boccard, M., Cheacharoen, R., Mailoa, J.P., McMeekin, D.P., Hoye, R.L.Z., Bailie, C.D., Leijtens, T., et al. (2017). 23.6%-efficient monolithic perovskite/silicon tandem solar cells with improved stability. Nat. Energy *2*, 23–26. https://doi.org/10.1038/nenergy.2017.910.1038/nenergy.2017.9.

11. Sahli, F., Werner, J., Kamino, B.A., Bräuninger, M., Monnard, R., Paviet-Salomon, B., Barraud, L., Ding, L., Diaz Leon, J.J., Sacchetto, D., et al. (2018). Fully textured monolithic perovskite/silicon tandem solar cells with 25.2% power conversion efficiency. Nat. Mater. *17*, 820–826. https://doi.org/10.1038/s41563-018-0115-410.1038/s41563-018-0115-4.

12. Mazzarella, L., Lin, Y.-H., Kirner, S., Morales-Vilches, A.B., Korte, L., Albrecht, S., Crossland, E., Stannowski, B., Case, C., Snaith, H.J., et al. (2019). Infrared light management using a nanocrystalline silicon oxide interlayer in monolithic perovskite/silicon heterojunction tandem solar cells with efficiency above 25%. Adv. Energy Mater. *9*, 1803241. https://doi.org/10.1002/aenm.20180324110.1002/aenm.201803241.

13. Liu, J., Aydin, E., Yin, J., De Bastiani, M., Isikgor, F.H., Rehman, A.U., Yengel, E., Ugur, E., Harrison, G.T., Wang, M., et al. (2021). 28.2%-efficient, outdoor-stable perovskite/silicon tandem solar cell. Joule *5*, 3169–3186. https://doi.org/10.1016/j.joule.2021.11.00310.1016/j.joule.2021.11.003.

14. Leijtens, T., Bush, K.A., Prasanna, R., and McGehee, M.D. (2018). Opportunities and challenges for tandem solar cells using metal halide perovskite semiconductors. Nat. Energy *3*, 828–838. https://doi.org/10.1038/s41560-018-0190-410.1038/s41560-018-0190-4.

15. Noh, J.H., Im, S.H., Heo, J.H., Mandal, T.N., and Seok, S.I. (2013). Chemical management for colorful, efficient, and stable inorganic–organic hybrid nanostructured solar cells. Nano Lett *13*, 1764–1769. https://doi.org/10.1021/nl400349b10.1021/nl400349b.

16. Hoke, E.T., Slotcavage, D.J., Dohner, E.R., Bowring, A.R., Karunadasa, H.I., and McGehee, M.D. (2015). Reversible photo-induced trap formation in mixed-halide hybrid perovskites for photovoltaics. Chem. Sci. *6*, 613–617. https://doi.org/10.1039/c4sc03141e10.1039/C4SC03141E.

17. Palmstrom, A.F., Eperon, G.E., Leijtens, T., Prasanna, R., Habisreutinger, S.N., Nemeth, W., Gaulding, E.A., Dunfield, S.P., Reese, M., Nanayakkara, S., et al. (2019). Enabling flexible all-perovskite tandem solar cells. Joule *3*, 2193–2204. https://doi.org/10.1016/j.joule.2019.05.00910.1016/j.joule.2019.05.009.

18. Eperon, G.E., Stone, K.H., Mundt, L.E., Schloemer, T.H., Habisreutinger, S.N., Dunfield, S.P., Schelhas, L.T., Berry, J.J., and Moore, D.T. (2020). The role of dimethylammonium in bandgap modulation for stable halide perovskites. ACS Energy Lett *5*, 1856–1864. https://doi.org/10.1021/acsenergylett.0c0087210.1021/acsenergylett.0c00872.

19. Bush, K.A., Frohna, K., Prasanna, R., Beal, R.E., Leijtens, T., Swifter, S.A., and McGehee, M.D. (2018). Compositional engineering for efficient wide band gap perovskites with improved stability to photoinduced phase segregation. ACS Energy Lett *3*, 428–435. https://doi.org/10.1021/acsenergylett.7b0125510.1021/acsenergylett.7b01255.

20. Abdi-Jalebi, M., Andaji-Garmaroudi, Z., Cacovich, S., Stavrakas, C., Philippe, B., Richter, J.M., Alsari, M., Booker, E.P., Hutter, E.M., Pearson, A.J., et al. (2018). Maximizing and stabilizing luminescence from halide perovskites with potassium passivation. Nature *555*, 497–501. https://doi.org/10.1038/nature2598910.1038/nature25989.

21. Zhou, Y., Jia, Y.-H., Fang, H.-H., Loi, M.A., Xie, F.-Y., Gong, L., Qin, M.-C., Lu, X.-H., Wong, C.-P., and Zhao, N. (2018). Composition-tuned wide bandgap perovskites: From grain engineering to stability and performance improvement. Adv. Funct. Mater. *28*, 1803130. https://doi.org/10.1002/adfm.20180313010.1002/adfm.201803130.

22. Azpiroz, J.M., Mosconi, E., Bisquert, J., and De Angelis, F. (2015). Defect migration in methylammonium lead iodide and its role in perovskite solar cell operation. Energy Environ. Sci. *8*, 2118–2127. https://doi.org/10.1039/c5ee01265a10.1039/C5EE01265A.

23. Walsh, A., and Stranks, S.D. (2018). Taking control of ion transport in halide perovskite solar cells. ACS Energy Lett *3*, 1983–1990. https://doi.org/10.1021/acsenergylett.8b0076410.1021/acsenergylett.8b00764.

24. Liu, X., Chen, Y., Miao, Y., Wei, N., Chen, H., Qin, Z., Feng, M., Wang, Y., Wang, X., and Zhao, Y. (2022). Stable pure iodide $MA_{0.95}Cs_{0.05}PbI_3$ perovskite toward efficient 1.6 eV bandgap photovoltaics. J. Phys. Chem. Lett. *13*, 5088–5093. https://doi.org/10.1021/acs.jpclett.2c0135610.1021/acs.jpclett.2c01356.

25. Eperon, G.E., Paternò, G.M., Sutton, R.J., Zampetti, A., Haghighirad, A.A., Cacialli, F., and Snaith, H.J. (2015). Inorganic caesium lead iodide perovskite solar cells. J. Mater. Chem. A *3*, 19688–19695. https://doi.org/10.1039/c5ta06398a10.1039/C5TA06398A.

26. Li, Z., Yang, M., Park, J.-S., Wei, S.-H., Berry, J.J., and Zhu, K. (2016). Stabilizing perovskite structures by tuning tolerance factor: formation of formamidinium and cesium lead iodide solid-state alloys. Chem. Mater. *28*, 284–292. https://doi.org/10.1021/acs.chemmater.5b0410710.1021/acs.chemmater.5b04107.

27. Ke, W., Spanopoulos, I., Stoumpos, C.C., and Kanatzidis, M.G. (2018). Myths and reality of $HPbI_3$ in halide perovskite solar cells. Nat. Commun. *9*, 4785. https://doi.org/10.1038/s41467-018-07204-y10.1038/s41467-018-07204-y.

28. Shao, Z., Meng, H., Du, X., Sun, X., Lv, P., Gao, C., Rao, Y., Chen, C., Li, Z., Wang, X., et al. (2020). Cs_4PbI_6-mediated synthesis of thermodynamically stable $FA_{0.15}Cs_{0.85}PbI_3$ perovskite solar cells. Adv. Mater. *32*, e2001054. https://doi.org/10.1002/adma.20200105410.1002/adma.202001054.

29. Meng, H., Shao, Z., Wang, L., Li, Z., Liu, R., Fan, Y., Cui, G., and Pang, S. (2020). Chemical composition and phase evolution in DMAI-derived inorganic perovskite solar cells. ACS Energy Lett *5*, 263–270. https://doi.org/10.1021/acsenergylett.9b0227210.1021/acsenergylett.9b02272.

30. Wang, X., Chen, Y., Zhang, T., Wang, X., Wang, Y., Kan, M., Miao, Y., Chen, H., Liu, X., Wang, X., et al. (2021). Stable cesium-rich formamidinium/cesium pure-iodide

perovskites for efficient photovoltaics. ACS Energy Lett *6*, 2735–2741. https://doi.org/10.1021/acsenergylett.1c0101310.1021/acsenergylett.1c01013.

31. Matsui, T., Seo, J.-Y., Saliba, M., Zakeeruddin, S.M., and Grätzel, M. (2017). Room-temperature formation of highly crystalline multication perovskites for efficient, low-cost solar cells. Adv. Mater. *29*, 1606258. https://doi.org/10.1002/adma.20160625810.1002/adma.201606258.

32. Lee, J.-W., Kim, D.-H., Kim, H.-S., Seo, S.-W., Cho, S.M., and Park, N.-G. (2015). Formamidinium and cesium hybridization for photo- and moisture-stable perovskite solar cell. Adv. Energy Mater. *5*, 1501310. https://doi.org/10.1002/aenm.20150131010.1002/aenm.201501310.

33. Kim, M., Kim, G.-H., Lee, T.K., Choi, I.W., Choi, H.W., Jo, Y., Yoon, Y.J., Kim, J.W., Lee, J., Huh, D., et al. (2019). Methylammonium chloride induces intermediate phase stabilization for efficient perovskite solar cells. Joule *3*, 2179–2192. https://doi.org/10.1016/j.joule.2019.06.01410.1016/j.joule.2019.06.014.

34. McMeekin, D.P., Sadoughi, G., Rehman, W., Eperon, G.E., Saliba, M., Hörantner, M.T., Haghighirad, A., Sakai, N., Korte, L., Rech, B., et al. (2016). A mixed-cation lead mixed-halide perovskite absorber for tandem solar cells. Science *351*, 151–155. https://doi.org/10.1126/science.aad584510.1126/science.aad5845.

35. Xie, F., Chen, C.-C., Wu, Y., Li, X., Cai, M., Liu, X., Yang, X., and Han, L. (2017). Vertical recrystallization for highly efficient and stable formamidinium-based inverted-structure perovskite solar cells. Energy Environ. Sci. *10*, 1942–1949. https://doi.org/10.1039/c7ee01675a10.1039/C7EE01675A.

36. Yu, H., Wang, F., Xie, F., Li, W., Chen, J., and Zhao, N. (2014). The role of chlorine in the formation process of "$CH_3NH_3PbI_{3-x}Cl_x$" perovskite. Adv. Funct. Mater. *24*, 7102–7108. https://doi.org/10.1002/adfm.20140187210.1002/adfm.201401872.

37. Yin, W.-J., Yan, Y., and Wei, S.-H. (2014). Anomalous alloy properties in mixed halide perovskites. J. Phys. Chem. Lett. *5*, 3625–3631. https://doi.org/10.1021/jz501896w10.1021/jz501896w.

38. Dar, M.I., Arora, N., Gao, P., Ahmad, S., Grätzel, M., and Nazeeruddin, M.K. (2014). Investigation Regarding the role of chloride in organic–inorganic halide perovskites obtained from chloride containing precursors. Nano Lett *14*, 6991–6996. https://doi.org/10.1021/nl503279x10.1021/nl503279x.

39. Li, J., Yu, Q., He, Y., Stoumpos, C.C., Niu, G., Trimarchi, G.G., Guo, H., Dong, G., Wang, D., Wang, L., et al. (2018). $Cs_2PbI_2Cl_2$, all-inorganic two-dimensional Ruddlesden–Popper mixed halide perovskite with optoelectronic response. J. Am. Chem. Soc. *140*, 11085–11090. https://doi.org/10.1021/jacs.8b0604610.1021/jacs.8b06046.

40. Kim, D.H., Muzzillo, C.P., Tong, J., Palmstrom, A.F., Larson, B.W., Choi, C., Harvey, S.P., Glynn, S., Whitaker, J.B., Zhang, F., et al. (2019). Bimolecular additives improve wide-band-gap perovskites for efficient tandem solar cells with CIGS. Joule *3*, 1734–1745. https://doi.org/10.1016/j.joule.2019.04.01210.1016/j.joule.2019.04.012.

41. Khenkin, M.V., Katz, E.A., Abate, A., Bardizza, G., Berry, J.J., Brabec, C., Brunetti, F., Bulović, V., Burlingame, Q., Di Carlo, A., et al. (2020). Consensus statement for stability assessment and reporting for perovskite photovoltaics based on ISOS procedures. Nat. Energy *5*, 35–49. https://doi.org/10.1038/s41560-019-0529-510.1038/s41560-019-0529-5.

42. Saliba, M., Matsui, T., Seo, J.-Y., Domanski, K., Correa-Baena, J.-P., Nazeeruddin, M.K., Zakeeruddin, S.M., Tress, W., Abate, A., Hagfeldt, A., et al. (2016). Cesium-containing triple cation perovskite solar cells: improved stability, reproducibility and high efficiency. Energy Environ. Sci. *9*, 1989–1997. https://doi.org/10.1039/c5ee03874j10.1039/C5EE03874J.

43. Boyd, C.C., Cheacharoen, R., Bush, K.A., Prasanna, R., Leijtens, T., and McGehee, M.D. (2018). Barrier design to prevent metal-induced degradation and improve thermal stability in perovskite solar cells. ACS Energy Lett *3*, 1772–1778. https://doi.org/10.1021/acsenergylett.8b0092610.1021/acsenergylett.8b00926.

44. Park, I.J., Kim, D.H., Ji, S.G., Ahn, Y.J., Park, S.J., Kim, D., Shin, B., and Kim, J.Y. (2021). Rationally designed window layers for high efficiency perovskite/Si tandem solar cells. Adv. Optical Mater. *9*, 2100788. https://doi.org/10.1002/adom.20210078810.1002/adom.202100788.

45. Gupta, R., Korukonda, T.B., Gupta, S.K., Dhamaniya, B.P., Chhillar, P., Datt, R., Vashishtha, P., Gupta, G., Gupta, V., Srivastava, R., et al. (2020). Room temperature synthesis of perovskite ($MAPbI_3$) single crystal by anti-solvent assisted inverse temperature crystallization method. J. Cryst. Growth *537*, 125598. https://doi.org/10.1016/j.jcrysgro.2020.12559810.1016/j.jcrysgro.2020.125598.

46. Maculan, G., Sheikh, A.D., Abdelhady, A.L., Saidaminov, M.I., Haque, M.A., Murali, B., Alarousu, E., Mohammed, O.F., Wu, T., and Bakr, O.M. (2015). $CH_3NH_3PbCl_3$ single crystals: inverse temperature crystallization and visible-blind UV-photodetector. J. Phys. Chem. Lett. *6*, 3781–3786. https://doi.org/10.1021/acs.jpclett.5b0166610.1021/acs.jpclett.5b01666.